



Experimental observation of wave localization at the Dirac frequency in a two-dimensional photonic crystal microcavity

LEI HU,¹ KANG XIE,^{1,5} ZHIJIA HU,^{1,2,3,6} QIUPING MAO,⁴ JIANGYING XIA,¹ HAIMING JIANG,¹ JUNXI ZHANG,¹ JIANXIANG WEN,³ AND JINGJING CHEN¹

¹*School of Instrument Science and Opto-electronics Engineering, Hefei University of Technology, Hefei, Anhui 230009, China*

²*Aston Institute of Photonic Technologies, Aston University, Birmingham B4 7ET, UK*

³*Key Laboratory of Specialty Fiber Optics and Optical Access Networks, Shanghai University, Shanghai, 200072, China*

⁴*College of Life Information Science and Instrument Engineering, Hangzhou Dianzi University, Hangzhou, Zhejiang 310018, China*

⁵*kangxie@hfut.edu.cn*

⁶*zhijiahu@hfut.edu.cn*

Abstract: Trapping light within cavities or waveguides in photonic crystals is an effective technology in modern integrated optics. Traditionally, cavities rely on total internal reflection or a photonic bandgap to achieve field confinement. Recent investigations have examined new localized modes that occur at a Dirac frequency that is beyond any complete photonic bandgap. We design Al₂O₃ dielectric cylinders placed on a triangular lattice in air, and change the central rod size to form a photonic crystal microcavity. It is predicted that waves can be localized at the Dirac frequency in this device without photonic bandgaps or total internal reflections. We perform a theoretical analysis of this new wave localization and verify it experimentally. This work paves the way for exploring localized defect modes at the Dirac point in the visible and infrared bands, with potential applicability to new optical devices.

© 2018 Optical Society of America under the terms of the [OSA Open Access Publishing Agreement](#)

OCIS codes: (230.5298) Photonic crystals; (140.3945) Microcavities; (350.4010) Microwaves.

References and links

1. J. Limpert, A. Liem, M. Reich, T. Schreiber, S. Nolte, H. Zellmer, A. Tünnermann, J. Broeng, A. Petersson, and C. Jakobsen, "Low-nonlinearity single-transverse-mode ytterbium-doped photonic crystal fiber amplifier," *Opt. Express* **12**(7), 1313–1319 (2004).
2. V. Lousse, W. Suh, O. Kilic, S. Kim, O. Solgaard, and S. Fan, "Angular and polarization properties of a photonic crystal slab mirror," *Opt. Express* **12**(8), 1575–1582 (2004).
3. J. Limpert, T. Schreiber, S. Nolte, H. Zellmer, T. Tünnermann, R. Iliew, F. Lederer, J. Broeng, G. Vienne, A. Petersson, and C. Jakobsen, "High-power air-clad large-mode-area photonic crystal fiber laser," *Opt. Express* **11**(7), 818–823 (2003).
4. L. Rindorf, J. B. Jensen, M. Dufva, L. H. Pedersen, P. E. Højby, and O. Bang, "Photonic crystal fiber long-period gratings for biochemical sensing," *Opt. Express* **14**(18), 8224–8231 (2006).
5. O. Frazão, J. L. Santos, F. M. Araújo, and L. A. Ferreira, "Optical sensing with photonic crystal fibers," *Laser Photonics Rev.* **2**(6), 449–459 (2008).
6. C. Wiesmann, K. Bergeneck, N. Linder, and U. T. Schwarz, "Photonic crystal LEDs—designing light extraction," *Laser Photonics Rev.* **3**(3), 262–286 (2009).
7. Y. Akahane, T. Asano, B.-S. Song, and S. Noda, "Fine-tuned high-Q photonic-crystal nanocavity," *Opt. Express* **13**(4), 1202–1214 (2005).
8. M. Notomi, A. Shinya, S. Mitsugi, E. Kuramochi, and H. Ryu, "Waveguides, resonators and their coupled elements in photonic crystal slabs," *Opt. Express* **12**(8), 1551–1561 (2004).
9. J. D. Joannopoulos, P. R. Villeneuve, and S. Fan, "Photonic crystals: putting a new twist on light," *Nature* **386**(6621), 143–149 (1997).
10. M. Diem, T. Koschny, and C. M. Soukoulis, "Transmission in the vicinity of the Dirac point in hexagonal photonic crystals," *Physica B* **405**(14), 2990–2995 (2010).
11. B. Wunsch, F. Guinea, and F. Sols, "Dirac-point engineering and topological phase transitions in honeycomb optical lattices," *New J. Phys.* **10**(10), 103027 (2008).
12. H. M. Guo and M. Franz, "Topological insulator on the kagome lattice," *Phys. Rev. B* **80**(11), 113102 (2009).

13. A. H. Castro Neto, F. Guinea, N. M. R. Peres, K. S. Novoselov, and A. K. Geim, "The electronic properties of graphene," *Rev. Mod. Phys.* **81**(1), 109–162 (2009).
14. S. Longhi, "Quantum - optical analogies using photonic structures," *Laser Photonics Rev.* **3**(3), 243–261 (2009).
15. X. Zhang, "Observing Zitterbewegung for photons near the Dirac point of a two-dimensional photonic crystal," *Phys. Rev. Lett.* **100**(11), 113903 (2008).
16. Y. Zhang, Y. W. Tan, H. L. Stormer, and P. Kim, "Experimental observation of the quantum Hall effect and Berry's phase in graphene," *Nature* **438**(7065), 201–204 (2005).
17. R. A. Sepkhanov, Y. B. Bazaliy, and C. W. J. Beenakker, "Extremal transmission at the Dirac point of a photonic band structure," *Phys. Rev. A* **75**(6), 063813 (2007).
18. K. Xie, H. Jiang, A. D. Boardman, Y. Liu, Z. Wu, M. Xie, P. Jiang, Q. Xu, M. Yu, and L. E. Davis, "Trapped photons at a Dirac point: a new horizon for photonic crystals," *Laser Photonics Rev.* **8**(4), 583–589 (2014).
19. K. Xie, A. D. Boardman, Q. Li, Z. Shi, H. Jiang, H. Xia, Z. Hu, J. Zhang, W. Zhang, Q. Mao, L. Hu, T. Yang, F. Wen, and E. Wang, "Spatial algebraic solitons at the Dirac point in optically induced nonlinear photonic lattices," *Opt. Express* **25**(24), 30349–30364 (2017).
20. K. Xie, W. Zhang, A. D. Boardman, H. Jiang, Z. Hu, Y. Liu, M. Xie, Q. Mao, L. Hu, Q. Li, T. Yang, F. Wen, and E. Wang, "Fiber guiding at the Dirac frequency beyond photonic bandgaps," *Light Sci. Appl.* **4**(6), e304 (2015).
21. M. Bellec, U. Kuhl, G. Montambaux, and F. Mortessagne, "Tight-binding couplings in microwave artificial graphene," *Phys. Rev. B* **88**(11), 115437 (2013).
22. U. Kuhl, S. Barkhofen, T. Tudorovskiy, H. J. Stöckmann, T. Hossain, L. de Forges de Parny, and F. Mortessagne, "Dirac point and edge states in a microwave realization of tight-binding graphene-like structures," *Phys. Rev. B* **82**(9), 094308 (2010).
23. M. Bellec, U. Kuhl, G. Montambaux, and F. Mortessagne, "Manipulation of edge states in microwave artificial graphene," *New J. Phys.* **16**(11), 113023 (2014).
24. S. Bittner, B. Dietz, M. Miski-Oglu, P. O. Iriarte, A. Richter, and F. Schäfer, "Observation of a Dirac point in microwave experiments with a photonic crystal modeling graphene," *Phys. Rev. B* **82**(1), 014301 (2010).
25. S. Bittner, B. Dietz, M. Miski-Oglu, and A. Richter, "Extremal transmission through a microwave photonic crystal and the observation of edge states in a rectangular Dirac billiard," *Phys. Rev. B* **85**(6), 064301 (2012).
26. J. Böhm, M. Bellec, F. Mortessagne, U. Kuhl, S. Barkhofen, S. Gehler, H. J. Stöckmann, I. Foulger, S. Gnutzmann, and G. Tanner, "Microwave Experiments Simulating Quantum Search and Directed Transport in Artificial Graphene," *Phys. Rev. Lett.* **114**(11), 110501 (2015).
27. J. Mei, Y. Wu, C. T. Chan, and Z. Q. Zhang, "First-principles study of Dirac and Dirac-like cones in phononic and photonic crystals," *Phys. Rev. B* **86**(3), 035141 (2012).
28. M. Plihal and A. A. Maradudin, "Photonic band structure of two-dimensional systems: The triangular lattice," *Phys. Rev. B Condens. Matter* **44**(16), 8565–8571 (1991).
29. K. Busch, S. Lölkes, R. B. Wehrspohn, and H. Föll, *Photonic Crystals: Advances in Design, Fabrication, and Characterization* (John Wiley & Sons, 2006).
30. R. Sepkhanov, *Light scattering by photonic crystals with a Dirac spectrum* (Leiden Univ. PhD thesis, 2009), pp. 25–27.
31. S. R. Zandbergen and M. J. A. de Dood, "Experimental observation of strong edge effects on the pseudodiffusive transport of light in photonic graphene," *Phys. Rev. Lett.* **104**(4), 043903 (2010).
32. S. Y. Lin and G. Arjavalingam, "Photonic bound states in two-dimensional photonic crystals probed by coherent-microwave transient spectroscopy," *J. Opt. Soc. Am. B* **11**(10), 2124–2127 (1994).

1. Introduction

Photonic crystals (PCs) are a kind of artificial material composed of periodic dielectric structures. They have been widely studied due to their theoretical value and engineering applications in recent decades. Their fascinating electromagnetic properties provide us with an ideal platform for controlling the propagation of waves in various fields such as photonic crystal fiber amplifiers [1], slab mirrors [2], fiber lasers [3], biochemical or optical sensors [4,5] and photonic crystal LEDs [6]. Meanwhile, PCs with defects that form cavities [7] or waveguides [8] are an efficient medium to confine light waves and realize localization of modes. The internal physical mechanism of trapping photons is traditionally attributed to photonic bandgaps or total internal reflections (TIR) [9]. The light field profiles of these modes obey an exponential energy decay in space. However, this restricts the future development of novel devices due to the high decay rate.

Recently, the Dirac point within the triangular series lattice [10–12] photonic band structures has attracted much attention due to the strong similar conical singularities in the electronic band structures of graphene [13]. This special band region with linear dispersion and linearly vanishing density of states leads to a set of quantum effects such as Klein tunneling [14], Zitterbewegung [15], the absence of Anderson localization [16] and pseudo-

diffusive transmission [17] in PC, in analogy with graphene. Two-dimensional (2D) localized modes in PC [18], 2D spatial algebraic solitons in nonlinear photonic lattices [19] and guided modes in photonic crystal fibers [20], have been studied near the Dirac frequency. The diverse approaches for photon capturing lead to an unusual algebraic decay of state and a unique frequency located beyond the bandgaps. However, these modes have not been identified experimentally.

Recently, two theoretical and experimental studies have been performed by building artificial graphene in the microwave domain: one with a honeycomb lattice of dielectric resonators [21–23] and the other with a triangular lattice of metallic rods [24,25]. Edge modes were found in these studies. Meanwhile, J. Böhm et al. [26] demonstrated the implementations of the continuous quantum wave search algorithms and directed wave transport in artificial graphene lattice. In this ingenious experiment, localized search states were brought into resonance with an extended lattice state near the Dirac point.

In this study, we experimentally demonstrate an inner cavity mode that is localized inside the lattice around a defect at the Dirac frequency. Since structures which operate in the visible and infrared light bands are quite difficult to manage due to their exquisite precision of dimension, the experiment is performed in the microwave bands where modern micro-fabrication technology is mature and complex periodic structures can be prepared with good precision. The dimensions of PCs can be scaled in proportion to any wavelength so that the results obtained in the microwave band are applicable to the visible and infrared bands. This work may lead to new theory and applications of guided waves.

2. Discussion of the problem

The Dirac point (Upper-right inset in Fig. 2) in the photonic band structure has a conical singularity with linearly vanishing density of states and linear dispersion in its vicinity. Maxwell's equations near the Dirac point can be reduced to the 2D massless Dirac

equation $-iv_D \left(\sigma_x \frac{\partial}{\partial x} + \sigma_y \frac{\partial}{\partial y} \right) \Psi = (\omega - \omega_D) \Psi$, where v_D is the group velocity, ω_D is the angular

Dirac frequency, σ_x and σ_y are Pauli matrices, and $\Psi = (\psi_1, \psi_2)^T$ represents the envelope amplitudes ψ_1, ψ_2 of a doublet of two degenerate Bloch states at the corners (K points) of the hexagonal first Brillouin zone [17,27]. The solution of this equation satisfies the relation $\psi_{1,2} \propto 1/(x + iy)^m$ at the Dirac frequency. By analyzing the general solutions of eigenstates in the vicinity of the K points, we can obtain the nontrivial cylindrical wave solution in the PC as $H_2 \propto r^{-m} \cdot J_M(Kr) e^{\pm i(M - m)\theta}$, ($M = 0, \pm 1, \pm 2, \pm 3, \dots$), where J_M is the M th order Bessel function, and θ is the azimuth angle varying from 0 to 2π [18]. When Kr is sufficiently large, the Bessel function J_M can be approximately expressed as $J_M(Kr) \approx 2(2\pi Kr)^{-1/2} \cos(Kr - \pi/4 - M\pi/2)$. It is easy to see that the amplitude of such modes decay algebraically at large distances in the form of $1/r^{m+1/2}$. Instead of existing in a complete bandgap, it settles at the Dirac frequency. The phase of the wave that passes through the origin jumps between $\pm \pi$ when the sign of the cosine term changes because the complex exponential terms are known in this range. Apparently, the wave is not a traveling wave but a standing wave. The above discussion explains the appearance of wave localization at the Dirac frequency in the PC, and confirms the algebraic profile of the modes. When we introduce a defect into this structure, the wave can exist around the defect as localized modes. Therefore, light confinement at the Dirac frequency is realized in agreement with theoretical considerations.

Prior to performing the experiments, some numerical calculations based on the well-known plane wave expansion (PWE) and finite difference time domain (FDTD) analysis [18,20,28] were performed to design the structure and acquire key parameters from the band structures and mode profiles. The detailed simulations and settings are presented in the following discussions.

3. 2D microwave PC design

A 2D microwave PC that consists of a triangular lattice of alumina ceramic (Al_2O_3) cylinders in air is designed. This material is transparent in the microwave frequency range, with a refractive index $n = 3.13$ and a very low loss factor at 10 GHz [29]. The analysis starts with an optimization of the Dirac cone of a 2D triangular lattice without defects, so as to establish the ratio of the cylinder width versus lattice constant, as well as the normalized frequency of the Dirac point. Then, a defect is introduced by changing the radius of a cylinder. The optimal parameter of the defect that supports well-confined modes at the Dirac frequency is determined. Finally, additional calculations are performed to study the special features of this structure. The edge states are discussed in the last section.

3.1 Optimizing the Dirac cone

An illustration of the top view of the 2D triangular lattice PC is shown in the lower-left inset of Fig. 1(a). The structure is composed of Al_2O_3 ($\epsilon_d \approx 9.8$) cylinders in air. The properties of the structure are determined by the lattice constant a , the ratio of the radius of the cylinders to the lattice constant r/a , and the refractive index n of the material. The ratio r/a affects the size of the Dirac cone and the location of the Dirac frequency. TE and TM band structures calculated using PWE for $r/a = 0.25$ are plotted in Fig. 1(a). A Dirac cone that satisfies the massless Dirac equation is found between $f_d a/c = 0.5163 \sim f_d a/c = 0.6664$ in the TE band structure. There is no Dirac cone found in the TM band structure, therefore, only the TE modes need to be considered. Variations of the Dirac cone edges and the Dirac frequency as the ratio r/a changes from 0.25 to 0.35 are shown in Fig. 1(b). The distance from the lower edge of Dirac cone to the Dirac point reaches its largest value of 0.225 when r/a is equal to 0.3. The normalized Dirac frequency at this point is $f_d a/c = 0.4763$. Because the lower margin of the Dirac cone is much smaller than the upper margin, it is a top priority in the optimization process. The value $r/a = 0.3$ is chosen for our experiment to achieve an adequate size for the lower margin.

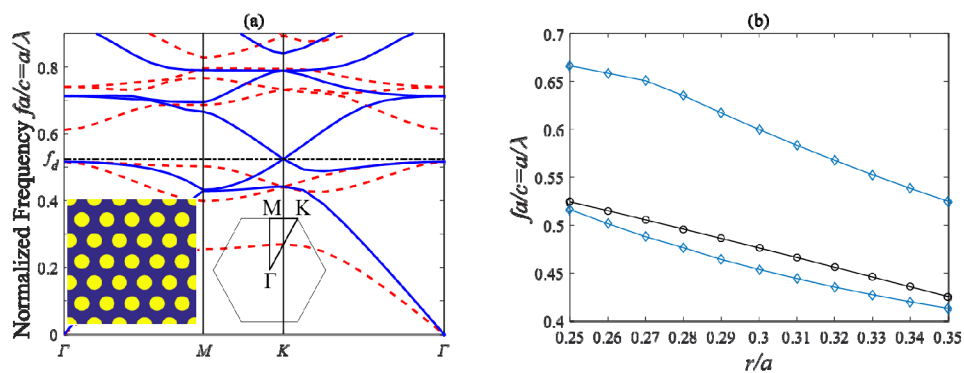


Fig. 1. (a) Calculated photonic band structure of a triangular lattice of dielectric rods in air. The rods are constituted of Al_2O_3 material with a dielectric constant $\epsilon_d = 9.8$ and a radius-to-pitch ratio $r/a = 0.25$. Blue lines: TE polarization. Red dashed lines: TM polarization. Black dot-dashed line at $f_d a/c = 0.5244$ marks the Dirac point in the TE band structure. Lower-left inset: top view of the 2D triangular lattice PC. Lower-middle inset: first Brillouin zone of the reciprocal lattice, revealing the high-symmetry points Γ , M , K at the corners of the irreducible Brillouin zone of the structure. (b) The variation of the Dirac cone edge with the radius-to-pitch ratio r/a . Blue diamond lines: Dirac cone edges. Black circle line: Dirac point.

3.2 Optimizing the defect size

A microcavity can be created by introducing a defect by altering either the radius or the relative permittivity of a single rod in the PC. For a practical device, it is more convenient to change the size of a cylinder instead of its inherent physical properties. Therefore, the radius

of an Al_2O_3 rod is modified to form the defect in this study. Localized modes are calculated by the PWE method in a 5×5 supercell system which includes a defect at the center. Figure 2 shows the dependence of the fundamental TE localized modes ($M = m = 1$) as the defect radius R changes. A localized Dirac mode appears near the Dirac frequency within the Dirac cone. The wave is confined in the PC and its energy is distributed nearby the defect rod. The mode, as shown in the lower-left inset of Fig. 2, resonates precisely at the Dirac frequency $f_d = 0.4763c/a$ when $R/r = 0.854$. The ratio of the two integers $6/7 = 0.857$ is in close proximity to the calculated ideal value R/r . Therefore, we set the diameter of the normal rods to $d = 7$ mm, and that of the defect rod to $D = 6$ mm. The lattice constant can be calculated as $a = d/0.6 = 11.67$ mm, the wavelength corresponding to the Dirac frequency as $\lambda = a/0.4763 = 24.5$ mm, and the Dirac frequency as $f_d = c/\lambda = 12.24$ GHz. The designed microwave PC will be further studied in experiments using these parameters.

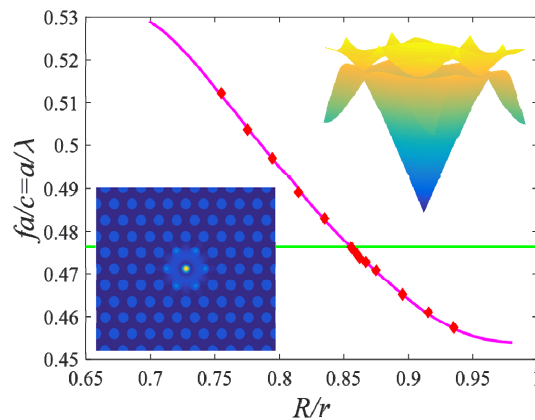


Fig. 2. Dependence of the frequency of the localized modes on the defect rod radius R . PC structure parameters are: $\epsilon_d = 9.8$, $r/a = 0.30$. Magenta solid curve: localized defect modes calculated by PWE method. Red diamonds: data points of the localized modes simulated by FDTD method. Green line: the Dirac point with the normalized frequency $f_d = 0.4763c/a$. Lower-left inset: profile of the localized modes at Dirac frequency superimposed on geometric structures of the crystals. Upper-right inset: conventional band structure in dimensionless frequency units. The Dirac cone is formed between the second and third photonic band for TE polarized waves.

3.3 Features of localized modes at Dirac point in microwave PC

To further confirm the rationale for designing the PC, 2D FDTD is applied to evaluate the resonant frequency, mode profile, phase on the profile, quality factor, and attenuation characteristics of localized modes. A $50 \text{ cm} \times 50 \text{ cm}$ microcavity, with 31×41 rods is analyzed. The detailed parameters are set as described in the previous section except for the defect size. A magnetic dipole source, which is not located in the defect's center, is used to excite the evolution of waves. The source is set with a short lifetime to ensure that the external source is timely switched off so that the dipole radiation couples freely. The dependence of the eigenfrequency of the localized mode with changes in the radius of the defect rod is plotted in Fig. 2. By appropriate adjustment of the defect radius, the resonance peak can be exactly moved to the Dirac frequency. This occurs at $D = 6.07$ mm, which results in a difference of only 1.2% compared to the result obtained using the PWE method. The results of our numerical computations are presented in Fig. 2 as red diamonds. Figure 3(a) shows the time-domain evolution of the magnetic field amplitude h_z at the center of the resonator. The field remains approximately constant with the progression of time, which ensures that such modes in the cavity are self-sustainable and that stable optical bound states are maintained. In Fig. 3(b) the pattern of frequency components of the magnetic field is

shown. The Gaussian pattern matches well with the result obtained using PWE, as shown by the inset in Fig. 2. The modulus of the frequency component $|H_z|$ multiplied by $r^{3/2}$ is plotted against distance r in Fig. 3(c). A relatively constant amplitude of oscillation occurs at the tail of the product $|H_z| \cdot r^{3/2}$, implying a $1/r^{3/2}$ algebraic decay rather than an exponential one for the mode. As seen from Fig. 3(d), the phase of the mode flips between $\pm \pi$ as distance changes, which implies a standing wave condition. The dependence of the quality factor Q_{total} of the cavity on the eigenfrequency of the mode is shown in Fig. 3(e). The Q factor achieves its maximum value of $\sim 6 \times 10^5$ at the Dirac frequency, and decreases rapidly as the frequency deviates from the Dirac frequency. These properties of the localized mode at the Dirac frequency are quite different from the traditional bandgap modes or TIR modes. Hence, the Dirac localized mode is a non-trivial alternative to the traditional bandgap modes, which has potentially meaningful applications.

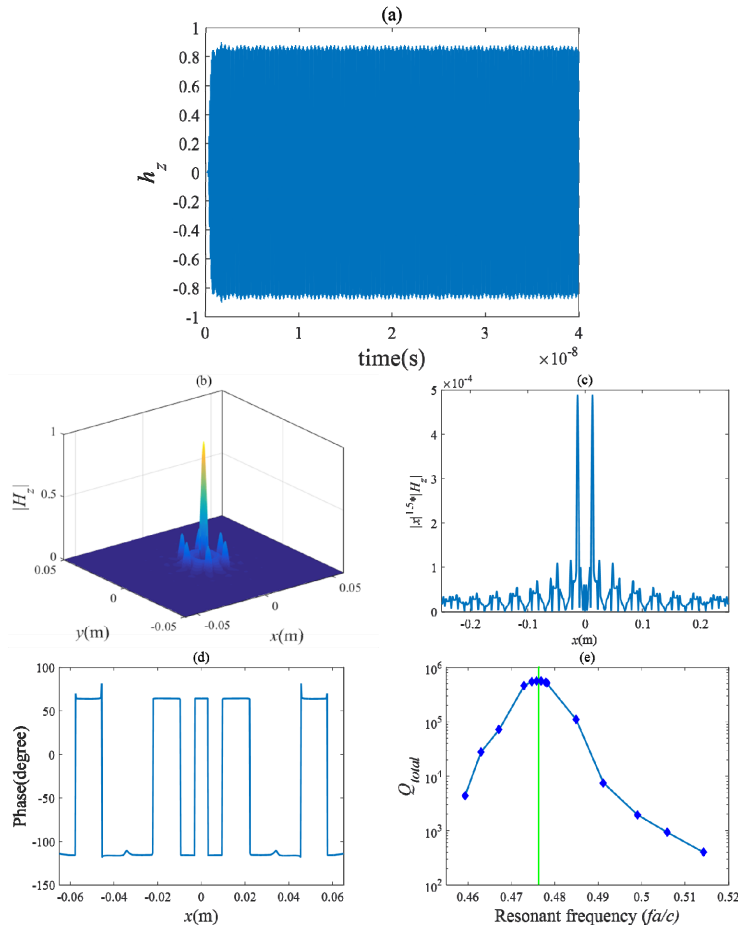


Fig. 3. Numerical investigations (by FDTD) of the Dirac mode at the Dirac frequency $f_d = 12.24$ GHz for the structure: lattice constant $a = 11.67$ mm, rods diameters $d = 7$ mm, defect diameter $D = 6$ mm, material relative permittivity $\epsilon_d = 9.8$ for both normal rods and the defect rod. The numerical computations are set with a step size $\Delta x = a/50$, $\Delta y = \Delta x \sin(60^\circ)$, time step $c\Delta t = 0.6484\Delta x$. Cavity area are $S = 50$ cm \times 50 cm, and the boundary conditions are PML boundary. (a) Time domain evolution of the magnetic field amplitude h_z at the cavity center. (b) Pattern of frequency component of the magnetic field $|H_z|$ at f_d . (c) Dependence of product of the $|H_z|$ and $r^{3/2}$ on the length in the x -axis. (d) Phase of the mode profile along the x axis. (e) Total quality factor Q_{total} variation with resonant frequency. The resonant frequency is dependent on the diameter D of the defect rod. The vertical green line marks the position of the Dirac frequency. The value of Q_{total} reaches its maximum at this frequency.

4. Experimental study

The measurement of the Dirac localized modes for complete PC is shown in Fig. 4. According to the design parameters and machining accuracy, dozens of Al_2O_3 dielectric cylinders are produced, for which the actual relative permittivity is 9.8 ± 0.7 and the cross-sectional diameter is 6.85 ± 0.1 mm. These rods are inserted between two layers of punched organic glass boards. The center-to-center distance of the holes is taken as 11.7 mm, and the hole diameter is 7 mm. This is larger than the rods size for easy insertion and removal. The space between the two boards is appropriately adjusted during the experiments. In order to incorporate a defect into the PC, the diameter of the central hole is reserved to be 6.1 mm, which is marginally larger than the designed diameter of the defect rod. To ensure the 2D nature of the structure [30,31], the rods are designed to be 200 mm long, which is much longer than the lattice constant of the crystal. In the PC shown in Fig. 1(a), localized modes at the Dirac frequency only occur for TE modes. For this polarization, a PC slab terminated by a perfect magnetic conductor on both ends at fixed z is equivalent to a 2D PC with an infinite length in the z direction. Unfortunately, perfect magnetic conductors do not exist. Nonetheless, the boundary conditions at the interface between two dielectric media with a large refractive index difference approaches that of the surface of a perfect magnetic conductor. The PC slab, which includes both cylinders and air spaces, can be considered as a bulk structure with an effective refractive index. Therefore, the PC slab with a finite thickness as previously shown with an open circuit on the z -axis, can be approximately considered as a

2D PC. The Maxwell equations of the TE wave are $\epsilon_0 \epsilon_r \frac{\partial E_x}{\partial t} = \frac{\partial H_z}{\partial y} - j_x$, $-\epsilon_0 \epsilon_r \frac{\partial E_y}{\partial t} = \frac{\partial H_z}{\partial x} + j_y$, $\mu_0 \frac{\partial H_z}{\partial t} = \frac{\partial E_x}{\partial y} - \frac{\partial E_y}{\partial x}$ for the 2D PC, where $j_{x,y}$ is the transverse

current density, which plays the role of the wave source. The electric current imported from the side of the PC excites the localized modes at the Dirac frequency. This structure is different from that of Refs [21–23,26], where the PCs are thin slabs with non-negligible thickness effects.

To obtain the range of the band gaps and the Dirac cone, horizontal transmission spectra of PCs are measured [30–32]. As shown in Fig. 4, the microwave signals produced by the analyzer are imported to the transmit antenna and they then pass through the PC, before finally flowing back to the ZVA40 through the receive antenna. The ZVA40 Vector Network Analyzer (Rohde & Schwarz) is used as the source to emit microwave signals through the transmit antennas, and the transmission spectra are collected via the receive antennas (WR - 62 Waveguide Standard Horn Antennas operating from 12 GHz to 18 GHz). The antennas are directly connected to two ports of the ZVA40. The boundaries of the PCs as well as the antennas are covered by the microwave absorbing materials. Thus, a long and narrow channel is formed to limit the receiving aperture of the antennas. Careful consideration should be exercised to minimize stray wave scattering and to maximize antenna directivity and detection efficiency. Appropriate adjustment of these settings allows the diffuse reflection, edge scattering, and incident wave from other directions to be effectively excluded. The radiation field is in an extent of the distance away from the PC, which can be viewed as satisfying the far-field condition. Therefore, the electromagnetic wave can strike the surface of PC perpendicularly in a particular direction.

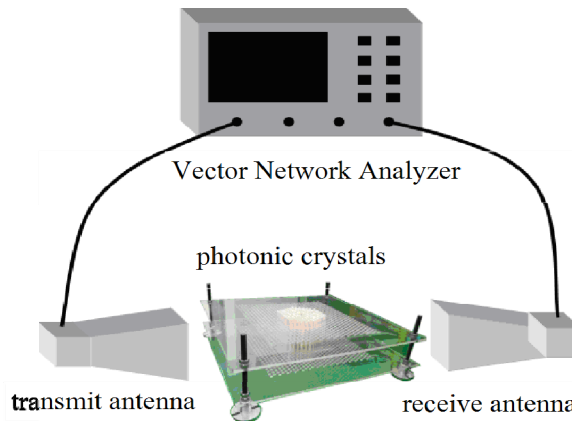


Fig. 4. Experimental setup for measurement of the transmission spectra of the PC cavity. Parameters of the cavity are: $a = 11.7$ mm, $\epsilon_d = 9.8 \pm 0.7$, $d = 6.85 \pm 0.1$ mm, and $D = 6$ mm.

The transmitted power of the TE polarization versus the frequency in the ΓM direction is plotted in Fig. 5(a). The TE band structure of the PC indicates that two partial bandgaps exist, which range from 11.66 to 15.41 GHz and 16.04–17.75 GHz along this direction, as shown in Fig. 5(b). Within the bandgaps, the fields decay exponentially with distance and the transmitted power is significantly attenuated in the aforementioned frequency ranges. This therefore indicates the position of bandgaps. The experimentally measured bandgaps are situated in the frequency ranges of 12.2–15.6 GHz and 16.2–17.3 GHz, which confirms the band structure calculations.

The measured spectra along the MK direction are shown in Fig. 5(c). Interestingly, the Dirac cone appears in this direction. S. Bittner et al. [24] proposed that an effective way to examine the Dirac point is to measure the frequency dependence of the transmitted (reflected) power. It was also shown that the transmitted power tends linearly to unity in the vicinity of the Dirac frequency. The band structure as shown in Fig. 5(d) reveals that partial stopband regions exist for 15.41 ~16.04 GHz and above 17.76 GHz, whereas the Dirac cone exists between 11.8 and 12.9 GHz. The transmittance of waves near the Dirac point obeys an unusual $1/L$ scaling law, namely, the law of pseudo diffusion [17]. The transmitted photon current near the Dirac point is therefore affected by the sample thickness. As a result, the transmitted power spectra exhibit a valley at the Dirac frequency, and the depth of the valley depends on the number of layers included in the sample.

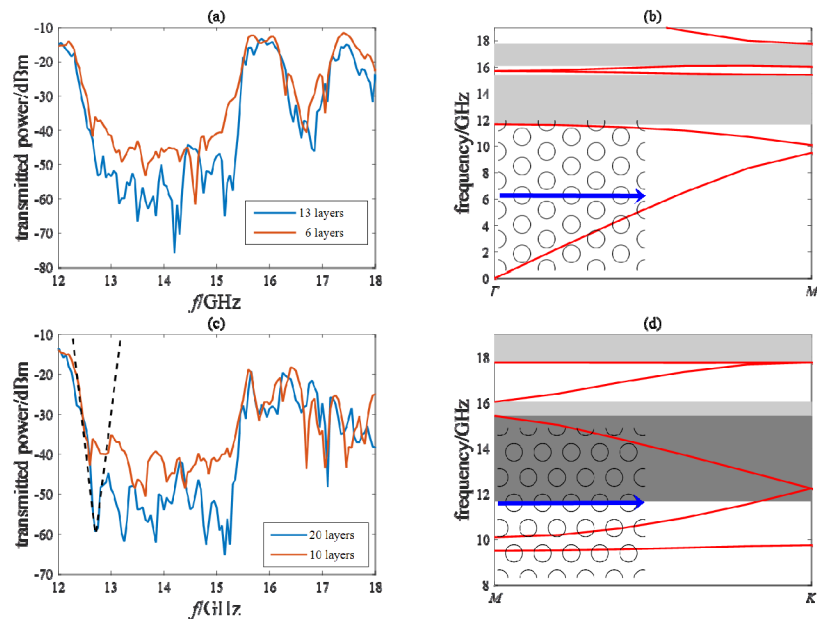


Fig. 5. (a) Transmitted power vs. frequency for the PC along ΓM direction with 6 or 13 layers in the propagation direction. (b) The band structure in the ΓM direction. The grey regions indicate two partial bandgaps within the effective frequency of the horn antennas. The lower-left inset shows the transmission direction. (c) Transmitted power vs. frequency for the PC along the MK direction with 10 or 20 layers in the propagation direction. The dashed lines mark the frequency range of the Dirac cone. (d) The band structure in the MK direction. The light grey regions indicate two partial bandgaps within the effective frequency of horn antennas. The dark grey region is the frequency range occupied by the Dirac cone. The lower-left inset shows the transmission direction.

By changing the size of the central cylinder, a point defect is incorporated into the PC. The transmitted power spectra of the PC with a defect rod of 5.9 mm in diameter is shown in Fig. 6(a). A comparison of the transmission spectrum shown in Fig. 5(a) without the defect with Fig. 6(a) reveals an extra peak in the latter corresponding to a defect mode at a frequency of 12.48 GHz. The FDTD simulations shown in Fig. 6(b) also exhibit a distinct peak in both the ΓM and MK directions at approximately 12.24 GHz. This is in agreement with the experimental measurements. The defect behaves as a resonant cavity; it introduces localized defect modes to the PC, so that the otherwise zero density of states at the Dirac point increases. A distinct transmission peak therefore occurs at the Dirac frequency due to the presence of the defect. The distinct resonant peak does not move when the transmission direction changes, which further confirms that this phenomenon is associated with localized defect states. This is because since the defect mode is isolated to a single part of the lattice, its Fourier representation is not characterized by any particular direction, so the same solution is found for all parts of the Brillouin zone.

An ideal model of the PC cavity extends to infinity in both the x and y dimensions. However, for a practical device as in our experiments, the periodic cladding must be terminated at some point. It is known that defect edge states appear at the Dirac frequency and its vicinity [22,23,25,26] depending on the precise shape of the edges. As such, when the localized modes at the Dirac frequency is discussed, we must consider the influence of the edges. In our actual system, the zigzag and armchair edges, which are parallel to ΓK and MK directions, respectively, are present [25]. In general, only the zigzag edge can support edge states. We found that both the edge and cavity states can exist near the Dirac frequency. However, just as in the case of a cavity state, the edge state has its own eigenfrequency that is usually different from the Dirac frequency. Only by special treatments, e.g., by adjusting the

refractive index or radius of the periodic rods, the eigenfrequency of the edge state can be made to coincide with the Dirac frequency. In our experiments, five edge states are found at 11.96, 12.19, 13.26, 14.28, and 14.81 GHz, while the eigenfrequency of the cavity state is tuned to the Dirac frequency of 12.24 GHz, so they are discriminable. Furthermore, the eigenfrequency of the edge state is fixed once the lattice is complete. It is noteworthy that the eigenfrequency of the cavity state depends on the parameters of the defect. The transmission peak is found to shift in position as the radius of the defect rod changes. To demonstrate this argument, we repeat the measurements for the defect rod of different diameters. The transmission peak is measured at 12.54, 12.48, and 12.39 GHz when the diameter of the defect rod is set to 5.8, 5.9, and 6.0 mm, respectively. This is convincing evidence that the measured peak near the Dirac frequency is associated with the cavity mode, rather than the edge modes.

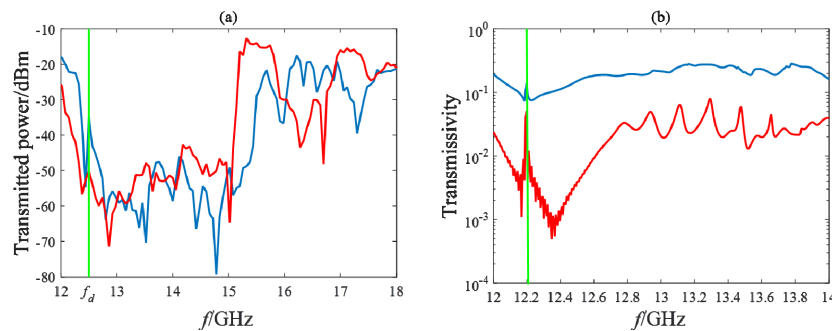


Fig. 6. (a) Transmitted power vs. frequency for the PC cavity with a defect. Red line: ΓM direction with 13 layers in the propagation direction. Blue line: MK direction with 19 layers in the transmission direction. The vertical green line marks the location of the resonant peak in both the ΓM and MK cases. (b) Numerically calculated (by FDTD) transmissivity of the photonic cavity with a defect (Red line: 13 layers on ΓM direction, blue line: 19 layers on MK direction). The vertical green line marks the location of the resonant peak in both the ΓM and MK cases.

In our experimental setup, incident waves from the air constitute an external source to the PC structure. For this configuration, edge states are hardly excited in the experiment. It is well-known that edge states are surface waves. Their dispersion curves lie below the light line. These waves are nonradioactive since there is a mismatch between their momentum values in air and at the edges. Moreover, the excitation of the edge states requires the use of internal sources near the edges [25,26]. In the previous FDTD simulations (Figs. 2 and 3), an inspection of the magnetic field profiles revealed that no edge state is excited, even in the presence of internal sources. This is because no eigenfrequency of the edge state for this experiment coincides with the Dirac frequency. As the eigenfrequency deviates from the Dirac frequency, the Q factor of the mode quickly decreases so that all the edge states are very lossy in this case. They are so leaky that energy from the internal dipole source cannot be accumulated sufficiently fast to form field patterns of the modes. This explains why no peaks are found at the eigenfrequencies of the edge states in the transmitted power spectrum in Fig. 6.

The dielectric constant of Al_2O_3 rod is assumed to have an empirical value of 9.8 in the design process, whereas in the actual manufacture and application stage, this value is allowed to vary between 9.8 ± 0.7 . The tolerance of the Dirac frequency on the errors of the dielectric constant of Al_2O_3 is analyzed. As observed in Fig. 7(a), the ± 0.7 variation in the dielectric constant of the sample results in a shift of the frequency of the Dirac point by 5%. Recalling that the measured transmission peak shown in Fig. 6(a) occurs at 12.48 GHz, while the FDTD simulated transmission peak shown in Fig. 6(b) occurs at 12.24 GHz, a discrepancy of approximately 2% still exists. The main cause of this discrepancy may be attributed to the

variation in the dielectric constant of the material. The uneven size of the dielectric cylinders is also taken into consideration during error analysis. Figure 7(b) shows the folded photonic band structure of a 5×5 supercell where the diameters of the 25 rods are set to uneven random values within 6.85 ± 0.1 mm. The standard photonic band structure of an ideal, uniform lattice for $d = 7$ mm is superimposed to show the original position of the Dirac frequency. It can be seen that the Dirac frequency remains almost unchanged as the diameter of the 25 rods of the supercell are unevenly varied and randomly varied by ± 0.1 mm near $d = 6.85$ mm. The position of the Dirac frequency is not sensitive to the rod size, which implies that the relative bias in the rod's dimensions does not significantly affect the experimental results.

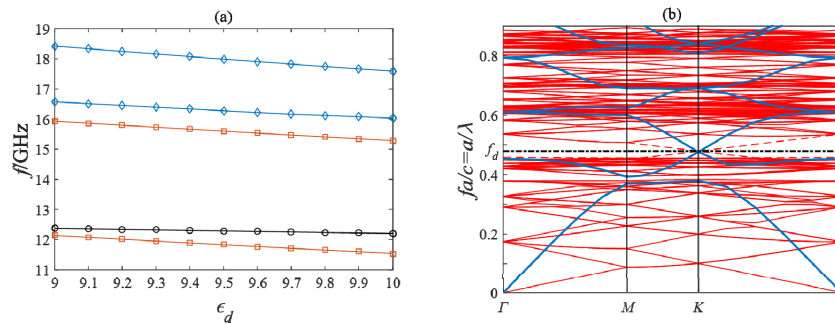


Fig. 7. (a) The partial bandgap edges and the Dirac point vary with the relative permittivity ϵ_d . Red rectangle lines: first partial gap edges in the ΓM direction as well as the Dirac cone edge. Blue diamond lines: second partial gap edges in the ΓM direction. Black circle line: Dirac point. (b) Red lines: Folded band structure of a 5×5 lattice with uneven rod sizes randomly varied between $d = 6.85 \pm 0.1$ mm. Blue lines: The standard photonic band structure of an ideal, uniform lattice for rod diameters $d = 7$ mm. The Dirac points (black dot-dashed line) for the two cases almost coincide with each other.

5. Summary

In summary, we designed a 2D microwave PC with a defect in the center, and calculated the localized cavity modes at the Dirac frequency. The transmission spectra of PCs with and without defects were measured experimentally. A resonant peak occurs at the Dirac frequency only when a defect is introduced. The frequency of the peak does not shift when the incident wave changes direction. No edge states are excited in this testing configuration. The experiment validated the existence of a Dirac mode, which is a localized cavity mode at the Dirac frequency. Although the experiment is performed in the microwave frequency range, it is scalable to any other electromagnetic frequency band. In addition, the particular properties of the Dirac mode were explained using PWE and FDTD.

Funding

National Natural Science Foundation of China (11574070, 11404087, 11404086, 51771186); Fundamental Research Funds for the Central Universities (JZ2017HGTD0187, PA2017GDQT0024); China Postdoctoral Science Foundation (2015M571918, 2017T100442); the European Union's Horizon 2020 research and innovation programme under the Marie Skłodowska-Curie grant agreement No 744817; STCSM; Natural Science Foundation of Anhui Province (1508085QA23).

Acknowledgments

The authors would like to thank Prof. Dr. Jun Yang for his help with the experiments.